Reconstructing 2-D Basement Relief Using Gravity Data by Deep Neuron Network: An Application on Poyang Basin

Rui Wang, Zhengwei Xu, Changjie Lai, Xuben Wang, Michael S. Zhdanov, *Member, IEEE*, Guowei Li, Zhiyao Cheng, Jun Li, Guangdong Zhao, Shengxian Liang, Hua Li, and Yuxin Zhang

***Abstract*— The stark contrast in density between geological layers is a fundamental aspect in the examination of basic geological structures. The delineation between the crystalline basement and sedimentary layers, moreover, is pivotal in the pursuit of strategic energy resources, such as petroleum and natural gas. Traditional full space density inversion, however, is beleaguered by issues of stability and resolution, impeding the accurate characterization of the sharp density interface. To rectify these shortcomings, we introduce an innovative methodology for estimating 2-D depth-to-basement and overlying density distribution, employing a deep neural network with a leaky rectified linear unit as an activation function. Evaluation of the proposed method on simulated sedimentary basin models underscores its superior ability to discern complex geometries of basin boundaries and overlying density, despite the presence of various degrees of Gaussian noise. In practical application to the Poyang basin, the relief of the Cretaceous basement is proficiently recovered through vertical gravity field data, with validation provided by corresponding seismic sections and well-established stratigraphic markers.**

***Index Terms*— Basement relief, deep neuron network, inversion, vertical gravity data.**

I. Introduction

THE configuration of a sedimentary basin serves as a potential record of its tectonic lineage, influencing the genesis, transit, and accumulation of hydrocarbons. As such, the elucidation of depth variation and undulation within the underlying basement constitutes an integral facet of regional tectonic investigation and hydrocarbon prospecting. Recognizably, vertical gravity anomalies, when measured, are frequently employed to discern the corresponding basement relief, assuming a significant density differential between the foundational strata and overlying sedimentary deposits.

Transposing low-dimensional anomalous gravity data into high-dimensional realistic density models frequently yields insights into the bottom relief of the basin. During the preliminary stages of exploration, 1-D or 2-D Bouguer gravity anomaly data are commonly employed as an initial method for scrutinizing the rudimentary geological structure. Nevertheless, this approach necessitates supplementary information concerning the depth of the sediment-basement interface [1]. A widely adopted human-assisted technique, trial-and-error, is utilized extensively to illustrate 2-D basement relief and density distribution by reconciling observed and predicted 1-D Bouguer gravity data [2], [3]. Despite its ubiquity, the method's demand for human interaction at each iteration phase makes it considerably time-intensive. Furthermore, its ability to concurrently manage thousands of grids to uphold the genuine geological structure is constrained.

As the field gravitates away from labor-intensive and often iterative methodologies, the endeavor to estimate subsurface density distribution has increasingly embraced machine-oriented gravity inversion techniques, such as gradient-type [4], [5], [6] and Monte Carlo type [7], [8]. Pallero et al. [9] performed a model evaluation of basement relief via a 2-D gravity inversion using particle swarm optimizers. Subsequently, Ekinci et al. [10] leveraged a differential evolution algorithm to invert the sedimentary basement through global optimization, thereby augmenting the efficiency of the algorithm. In pursuit of capturing the quintessential blocky geological structures found in nature, geophysical scholars have proposed numerous techniques under determinacy to augment the detectability of "smooth" borders. For instance, some inversion frameworks consider portraying basin structures based on a singular type of physical property, including total variation [11], [12], minimum gradient support [13], and multinary inversion [14]. The development of multiproperty-based inversion has paved the way for discerning basement structures with sharper boundaries, such as cross-gradients

Manuscript received 15 September 2022; revised 26 January 2023 and 24 May 2023; accepted 4 December 2023. Date of publication 7 December 2023; date of current version 29 December 2023. This work was supported in part by the Natural Science Foundation of Jilin Province under Grant 20200201053JC and in part by the Innovation and Development Strategy Research Project of Science and Technology Department of Jilin Province under Grant 20220601157FG. *(Corresponding author: Zhengwei Xu.)*

Rui Wang, Guowei Li, Zhiyao Cheng, Hua Li, and Yuxin Zhang are with School of Computer Science and Technology, the Changchun University of Science and Technology, Changchun 130022, China (e-mail: rwang@cust.edu.cn; 13283829343@163.com; zhiyaocheng@mails.cust.edu.cn; lihua@cust.edu.cn; zhangyuxin25@126.com).

Zhengwei Xu, Xuben Wang, Jun Li, Guangdong Zhao, and Shengxian Liang are with the College of Geophysics and the Key Laboratory of Earth Exploration and Information Techniques, Ministry of Education, Chengdu University of Technology, Chengdu 610059, China (e-mail: zhengwei.xu@cdut.edu.cn; wxb@cdut.edu.cn; lijun3@cdut.edu.cn; guangdongzhao@cdut.edu.cn; liangshengxian626@163.com).

Changjie Lai is with the Engineering Geology Brigade of Jiangxi Bureau of Geology, Nanchang 330001, China, and also with the Jiangxi Institute of Shale Gas Investigation and Development Research, Nanchang 330001, China (e-mail: laichangjie.0710@163.com).

Michael S. Zhdanov is with the Department of Geology and Geophysics, The University of Utah, Salt Lake City, UT 84107 USA.

Digital Object Identifier 10.1109/TGRS.2023.3340523

[15] and Gramian constraints [16]. Moreover, hybrid imaging approaches have been the subject of considerable focus in geophysical research to enhance the resolution of imaging basement relief [17], [18], [19].

Despite the prevalent deployment of sophisticated gravity inversion techniques to elucidate basin structures within geophysical exploration, it is evident that the mechanisms for identifying model perturbations rely heavily on both the theoretical gravity forward operator and the inversion algorithms previously mentioned [20]. For example, in cases where millions of subdivided grids are in play, complexities arise pertaining to the computation and storage of extensive matrices, thereby exacerbating the underdetermination and introducing instability.

Numerous methodologies have been conceptualized and executed to foster precision and stability in the realm of gravity-based basin relief interpretation. For instance, Elkins [21] delivered a compelling discourse, delineating both theoretical considerations and pragmatic applications of the second derivative methodology in gravitational interpretation, partially drawing upon antecedent work by Peters [22]. Therewith, employing the principle of successive approximation for eliminating residuals via a connected series of polygonal straight lines, Bott [23] offered a framework for determining 2-D shapes of sedimentary basins directly from gravity anomaly profiles. Nevertheless, the procedure exhibits optimal performance when the depths to the perturbing mass are insignificant relative to the distances separating observed anomalies. Oldenburg [24] initially introduced an iterative inversion methodology, which is grounded in a reinterpretation of Parker's formula [25] designed for swift computation of the gravitational anomaly attributable to an uneven layer. However, he posited that the method's convergence is achieved exclusively in particular instances where the gravitational anomaly can be ascribed to a layer with adequately minimal relief. Fedi and Rapolla [26] proposed a noniterative and nonlinear method for estimating basement morphology, which intriguingly permits the estimation of a constant density contrast through the juxtaposition of observed data with model-derived predictions. Yet, it is contingent on the knowledge or presumption of the basement's minimum and maximum depths. Florio [27] introduced a novel method for estimating basement morphology predicated on a straightforward relationship between basement depth and gravity or pseudo-gravity fields, with the precision of the method hinging on the accuracy of depth constraints.

The conceptual foundation of a backpropagation (BP) neural network, framed as a multilayer feed-forward neural network, was initially laid down by Hinton and McClelland [28]. This process entails two stages: forward propagation and error BP. The BP neural network aims to reconstruct subsurface geological anomalies by learning the inherent mapping associations between input data and the output model, thereby swiftly transforming observed geophysical data into an appropriately calibrated geological model [29]. A plethora of weight threshold optimization techniques have been proposed to predict basement relief using the BP neural network by employing genetic algorithms [30], [31]. A fusion of traditional inversion and pseudo-BP neural network computation was employed to discern the Tertiary basement and the Moho interface in the southern Okinawa trough basin [32]. However, this method necessitates an initial model incorporating prior geological information. While these two sophisticated optimization techniques are more aptly suited to local contexts as opposed to global ones, it is worth noting that the effective reconstruction of basement relief from gravity data via deep learning remains a relatively unexplored frontier in geophysical research.

This article endeavors to deploy a robust deep neural network (DNN) technique for the extraction of basement relief information from vertical gravity data. We put forward an efficient model generation approach, simulating two prototypical bottom relief training model sets that serve as reliable labels for the establishment of the deep learning network. By sectioning the sedimentary into a series of vertically adjacent prisms, we utilize a rapid modeling algorithm to generate credible training gravity datasets for the input end. Moreover, we introduce varying degrees of Gaussian noise to test the network's resilience to noise. The proposed imaging strategy is then applied to recover the relief of the Cretaceous basement using vertical gravity field data collected from the Poyang basin in China.

II. Methodology

A. 2-D Forward Modeling

Fig. 1 shows a schematic of a 2-D sedimentary basin model. For better simulation of theoretical geophysical response, the basin model is vertically divided into a set of M 2-D juxtaposed prims adjacent to each other, where the top surface coincides with the upper interface of the sedimentary layer, and the lower interface represents the basement relief. The gravity anomalies simulated at each observation point are contributed by all 2-D vertically juxtaposed prims, representing the effective response of density distribution and basement relief undulation. The vertical gravity, g_z, can be expressed as follows:

$$g_z^i = \sum_{j=1}^{M} f_i(\rho_j), \quad i = 1, 2, \ldots, N \tag{1}$$

where i represents the ith observation point, j stands for the jth 2-D prim, and f_i is defined as the forward function [33] as

$$f_i(\rho_j) = 2G \int_{b_{j1}}^{b_{j2}} \int_{a_{j1}}^{a_{j2}} \Delta\rho(z) \times \frac{a - z_i}{(b - x_i)^2 + (a - z_i)^2} \mathrm{d}a\mathrm{d}b \tag{2}$$

where a_{j1} and a_{j2} are defined as the horizontal boundaries along the x-axis. Similarly, b_{j1} and b_{j2} can be set up as the vertical boundaries along the z-direction [Fig. 2(b)]; G is the gravitational constant ($G = 6.67384 \times 10^{-11}\mathrm{m}^3/\mathrm{kg} \times \mathrm{s}^2$); and $\Delta\rho(z)$ represents the anomalous density. After integrating over b, the vertical gravity response can be acquired by combining with (1) and (2).

B. Generation of Sediment-Basement-Interface Training Sets

The purpose of constructing reasonable training sets is to enable the DNN to extract detailed features from low-dimensional input gravity data to establish an implicit

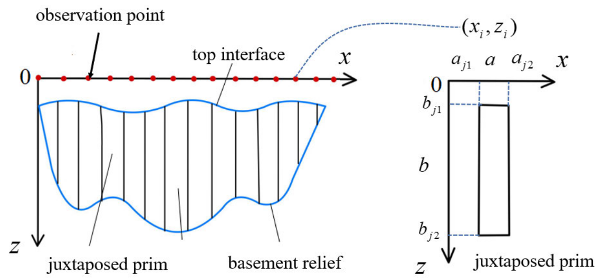

Fig. 1. Schematic of a 2-D sedimentary basin model.

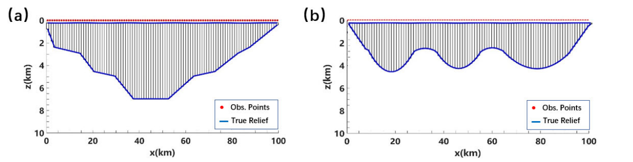

Fig. 2. Two types of basin models for the training: (a) terrain of rift sedimentary basin and (b) grab-horned sedimentary basin.

relationship with high-dimensional output-labeled basement models (e.g., relief and density). The random terrain of sedimentary rift basins [see Fig. 2(a)] and grab-horned basins [see Fig. 2(b)], as two kinds of typical basins, is designed under the guidance of empirical geological scenarios. The horizontal range along the x-axis is 0–100 000 m, and the depth range along the z-axis is 0–10 000 m. The number of slabs in each model is randomly selected from 1 to 5. The observation points are spaced at 1000-m intervals along the x-axis. The anomalous density filling within each prim varying with depth follows hyperbolic function [34] as given in the following:

$$\Delta\rho(z) = \frac{\Delta\rho_0 \times \beta^2}{(z+\beta)^2} \tag{3}$$

where $\Delta\rho_0$ is the density contrast at the surface; z is the depth of layers with anomalous density $\Delta\rho$; and β is the empirical constant with length units. In this article, to make sure the trained basin models are according to common knowledge of geology, we set up the variation of width and depth ratio $10 \leq W/H \leq 15$ as an additional constraint [35], where the relative error between geophysical responses from layered and compelling density models is about 2.5%.

In this study, we created 10 000 sets of training models, of which the depth information and empirical parameters β are used as scalar-trained labels as $\boldsymbol{O}(\psi) = \{\boldsymbol{z}^{\psi}, \boldsymbol{\beta}^{\psi}\}_{\psi=1}^{N}, N = 10\,000$. Subsequently, the corresponding gravity responses, as $\{\boldsymbol{g}_z^{\psi}\}_{\psi=1}^{N}, N = 10\,000$, are simulated by the forward modeling shown in (1) and (2), and the interior features are extracted from them to establish the inherent relationship with the labeled relief of the basement. We randomly choose 80% of the datasets for the neural network, and the rest are carried out for validation.

C. Deep Neuron Network

The DNN exhibits the proficiency to implicitly decipher complex and nonlinear input–output mode mappings by adjusting the thresholds and weights linked to neighboring network layers via the gradient descent method, without necessitating the explicit elucidation of the physical mathematical equations that depict the relationship. The regular diminution of dimensions at the terminal of the network model invariably results in the loss of feature information. Simultaneously, given that the data structure accommodated by the basement reliefs and overburden density constitutes an integrated 1-D matrix in this study, the quantities of neurons and hidden layers become pivotal elements in defining the architecture of the network.

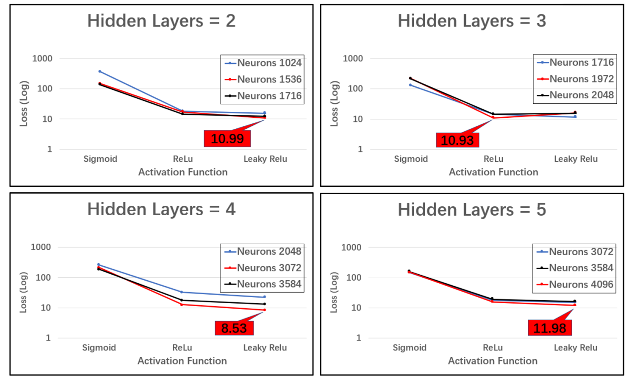

Fig. 3. Comparison of different hidden layers and loss behaviors.

Perceptrons, which are neural networks devoid of hidden layers, have demonstrated utility in addressing elementary geophysical classification challenges [36], [37], [38], yet their inherent limitations render them unsuitable for tackling more intricate geophysical problems. Although a neural network with a solitary hidden layer is theoretically capable of approximating any continuous function mapping one finite space to another [39], [40], this configuration may inadequately capture the complex nature of underlying physical processes and is susceptible to overfitting or underfitting the data. Consequently, incorporating additional hidden layers into a neural network bolsters its ability to represent complex input–output relationships, mitigate overfitting by learning generalized representations, potentially alleviate manual feature engineering in geophysical inversion challenges, and augment effectiveness in managing large, intricate datasets characterized by high-dimensional inputs and multivariate, correlated outputs. Hence, the prediction of basin depth ($\boldsymbol{z}$) and empirical constant with length units ($\boldsymbol{\beta}$) constitutes a quintessential nonlinear problem, prompting the establishment of a hidden layer count exceeding two.

In this assessment, the adopted DNN structure adheres to conventional deep network architecture, whereby the determination of the number of hidden layers, the optimal neuron count in each layer, and the confirmation of deep learning network hyperparameters via various activation functions are fine-tuned through an empirical evaluation approach, contingent upon the loss observed in the testing sets. The comparison is shown in Fig. 3.

One can see that the optimal neural network configuration for the given problem, considering the loss behavior of testing sets, consists of four hidden layers (Fig. 4) with 3072 neurons (Table I), employing the leaky rectified linear unit (ReLU) activation function. This configuration provides the lowest loss value (8.53) and demonstrates better performance and generalization ability compared to other configurations.

For nonlinear reconstruction of the depth-to-basement with density variation, activation functions play a crucial role in

TABLE I
NEURONS NUMBER IN HIDDEN LAYERS OF THE DEEP NEURON NETWORK

Layers	Neurons
1st hidden layer	512
2nd hidden layer	1024
3rd hidden layer	1024
4th hidden layer	512

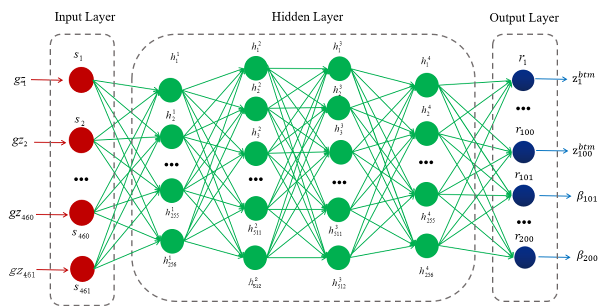

Fig. 4. Schematic of network structure.

training the artificial neural network to determine whether the extracted features that a specific neuron receives are helpful and whether they should be kept or discarded. Upon examining the efficacy of the preferred configuration of neural networks, it becomes evident that those employing ReLU and leaky ReLU activation functions surpass their sigmoid function counterparts. The sigmoid function can instigate the vanishing gradient issue, potentially leading to protracted convergence and diminished model accuracy. Conversely, ReLU and leaky ReLU serve to alleviate the vanishing gradient conundrum, fostering enhanced learning, and superior model performance. Comparing ReLU and leaky ReLU, the latter yields a reduced the lowest loss value, attributable to its introduction of a modest negative slope for negative input values, which assists in preserving gradients and diminishes the probability of encountering "dead neurons"—neurons producing zero output for all inputs, thereby rendering no contribution to the model's learning process. To conclude, the configuration demonstrates superior performance and generalization aptitude in comparison to alternate configurations sharing the same quantity of hidden layers and neurons. Therefore, the leaky ReLU is chosen as the activation function in this article rather than the ReLU because of the low sensitivity and scarcity of the vertical gravity training datasets.

In Fig. 4, the input layer for the ψth training set corresponds to 461 observation Bouguer gravity anomalies data points (e.g., $\boldsymbol{g}_z^{\psi} = [g_{z1}^{\psi}, g_{z2}^{\psi}, g_{z3}^{\psi}, \ldots, g_{z461}^{\psi}]^{\mathrm{T}}$) ranging from 0 to 100 km along the x-axis with a spacing of approximately 0.21 km. The input gravity information is received by neurons in the first layer, which then transmits it to neurons in the hidden layers. The output layer stands for depth-to-basement bottoms selected as the first output vector as $\boldsymbol{z} = [z_1^{\mathrm{btm}}, z_2^{\mathrm{btm}}, \ldots, z_{100}^{\mathrm{btm}}]^{\mathrm{T}}$, and the empirical parameters β shown in (3) as the second output vector as $\boldsymbol{\beta} = [\beta_1, \beta_2, \ldots, \beta_{100}]^{\mathrm{T}}$.

The loss function plays a significant role in acquiring the perturbation of the weights and thresholds inside the deep learning network. The loss function of the ψth training sets is defined as $\boldsymbol{E}(\psi)$

$$\boldsymbol{E}(\psi) = \frac{1}{2}\sum_{k=1}^{n}(\boldsymbol{T}_k(\psi) - \boldsymbol{O}_k(\psi))^2 \tag{4}$$

where $\boldsymbol{T}_k(\psi)$ is a scalar vector containing the true values of depth and β of the kth-dimension of the ψth trained labels. $\boldsymbol{O}_k(\psi)$ is the scalar vector presenting the predicted values of depth and β information based on the kth-dimension of the ψth trained model set. For any specific training sample g_{zm}^{ψ}, we typically employ the strategy of layer-by-layer derivation from the output layer to the input layer to obtain the perturbation values of the weights in each layer. The detailed derivation is given in the Appendix.

To alleviate the computational load associated with gradient calculations across an extensive dataset, especially for more sizable collections of data, the batch size is optimally defined, signifying a data subset that approximates the accurate gradient. Guided by various factors, including specific problem characteristics, the architecture of the model, the scale of the dataset, and the computational resources at disposal, the batch size in this study is selected from an ensemble comprising 16, 32, 64, 128, and 256. This choice, adhering to exponential powers of 2, capitalizes on the superior performance of the GPU relative to multiples of 10 or 100, given the GPU's constrained computational capacity during training. Empirical observations validate quick and steady convergence when a batch size of 256 is implemented.

The performance of underfitting and overfitting the model is the most logical way to evaluate the generalization capacity of the trained network structure. In general, underfitting can be reduced by modifying the training procedure or grid structure of the DNN, whose expressive ability is strong enough to make parameters surpass the minimal generalization misfit critical point of the training curves. The most popular regularization method for deep learning model training is dropout [41]. The determination of an optimal dropout rate is often empirically driven, necessitating a trial-and-error approach. This study adopted an initial low dropout rate of 0.1, progressively increasing it should overfitting persist. Nonetheless, caution is required to avoid excessive regularization leading to underfitting, which may occur with overly high dropout rates. The final dropout rate, offering an optimal balance, was found to be 0.2.

In striking an optimal balance between underfitting and overfitting, the number of epochs in training a model holds significant importance. Underfitting, a scenario where the model is inadequately trained and thus underperforms, may arise when the number of epochs is insufficient. Conversely, overfitting may ensue from excessive epochs, as the model becomes overly familiarized with the training data, including its noise and outliers, which degrades its performance on novel data. The optimum epoch count is typically derived empirically. A prevalent method involves tracking the model's performance on a validation set after each epoch. The practice of "early stopping" halts training when the validation set performance plateaus or begins to deteriorate. In this study, dynamic observation of the model's loss in the training and validation sets after each epoch revealed an increase in the validation set loss upon exceeding 4000 epochs during training. Consequently, training was ceased to circumvent model overfitting.

The comprehensive misfit levels for labels ($\text{misfit}^{\text{ML}_1}$ and $\text{misfit}^{\text{ML}_2}$) and gravity data ($\text{misfit}^{\text{DI}}$) are common ways to determine when to terminate BP and thus obtain the optimal solution, respectively. The misfit functions are defined as

$$\text{misfit}^{\text{DI}} = \frac{\left\| g_z^{\text{pred}} - g_z^{\text{obs}} \right\|_{\text{DI}}^2}{\left\| g_z^{\text{obs}} \right\|_{\text{DI}}^2} \tag{5}$$

$$\text{misfit}^{\text{ML}_1} = \frac{\left\| z^{\text{pred}} - z^{\text{label}} \right\|_{\text{ML}}^2}{\left\| z^{\text{label}} \right\|_{\text{ML}}^2} \tag{6}$$

$$\text{misfit}^{\text{ML}_2} = \frac{\left\| \beta^{\text{pred}} - \beta^{\text{label}} \right\|_{\text{ML}}^2}{\left\| \beta^{\text{label}} \right\|_{\text{ML}}^2} \tag{7}$$

where DI denotes the data space at the end of the input; ML_1 and ML_2 are denoted as two model labels at the end of the output, respectively; g_z^{pred} and g_z^{obs} stand for simulated and observed vertical gravity response, respectively; z^{pred} and z^{label} are defined as the first output type as basin interface depth and trained one, respectively; and β^{pred} and β^{label} are denoted as the second output type as the empirical parameters and corresponding trained one.

III. Synthetic Model Studies

Fig. 5 presents the relief results of three validated sedimentary basin models, arbitrarily selected from the 2000 validation datasets. It is observable that the interfaces of the graben-horned sedimentary basin, as reconstructed by the optimally-tuned weights and thresholds trained within the network, align effectively with the accurate models (signified by the black solid lines), as indicated by the overlaid black dashed lines. Additionally, the derived empirical parameter β [see (3)] employed for determining the density of each prim exhibits proximity to the actual value of the model. Concurrently, for each validated model, the vertical gravity responses generated by the reconstructed models (indicated by the red solid line) are superimposed with the observed responses (blue solid line). This visualization illustrates that the predicted gravity responses derived from the corresponding models faithfully adhere to the observed data.

Similarly, Fig. 6 represents the predicted interfaces of the rift sedimentary basin. The DNN can successfully recover all the sediment relief features and the corresponding empirical parameters β for each prim. We also discover that the fitting of the gravity curves is pretty good.

In order to evaluate the resilience of the trained network, zero-mean Gaussian noise, with a standard deviation calibrated to 5%, 10%, and 15% of the magnitude at each point, is incorporated into the observed gravity responses produced by the graben-horned and rift sedimentary basin models. Subsequently, the trained network is employed to reconstruct the relief and the parameter β from these noise-perturbed gravity responses. Figs. 7 and 8 showcase the congruity of observed and predicted gravity responses, as well as the inversion results under the influence of three distinct noise levels.

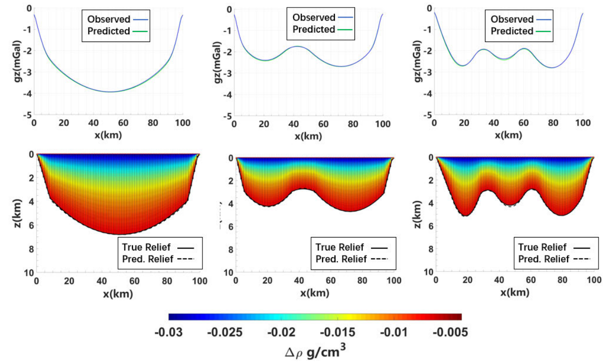

Fig. 5. (Top row) Comparison of predicted and observed vertical gravity g_z of three different graben-horned sedimentary basin models randomly selected from validation datasets. (Bottom row) Prediction, actual reliefs, and density transferred by the recovered empirical parameters β for the three corresponding graben-horned sedimentary basin models.

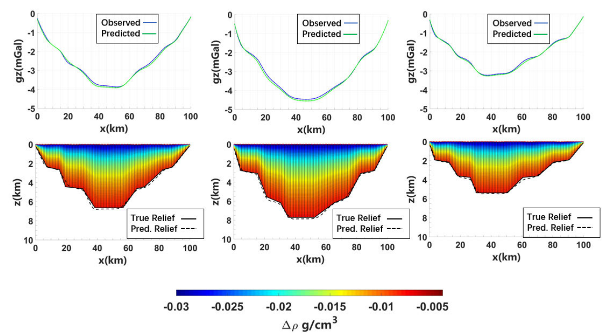

Fig. 6. (Top row) Comparison of predicted and observed vertical gravity g_z value for three different rift sedimentary basin models randomly selected from validation datasets. (Bottom row) Empirical parameters β of the three corresponding rift sedimentary basin models recovered from prediction and actual reliefs.

TABLE II

Misfit Errors and Training Time of the Gravity Responses (g_z), Depth-to-Basement Bottoms (z), and Empirical Parameters (β) for the Rift and Graben-Horned Sedimentary Models With Different Noise Levels

Error/Training Time	5% noise	10% noise	15% noise
$misfit^{DI}$ (rift)	1.03×10^{-3}	1.39×10^{-3}	1.45×10^{-3}
$misfit^{ML_1}$ (rift)	4.49×10^{-7}	5.47×10^{-7}	8.57×10^{-7}
$misfit^{ML_2}$ (rift)	4.43×10^{-7}	5.12×10^{-7}	6.47×10^{-7}
Train Time (rift)	3.37 min	3.30 min	3.24 min
$misfit^{DI}$ (graben-horned)	1.20×10^{-3}	1.30×10^{-3}	1.57×10^{-3}
$misfit^{ML_1}$ (graben-horned)	7.45×10^{-7}	8.09×10^{-7}	1.18×10^{-7}
$misfit^{ML_2}$ (graben-horned)	7.06×10^{-7}	7.85×10^{-7}	9.06×10^{-7}
Train Time(graben-horned)	3.97 min	3.88 min	3.64 min

As can be seen, the trained network is stable for noisy data and the proposed trained deep neuron network is still able to recover the model from the noise-contaminated data. The corresponding misfit fitting behaviors and training time of the g_z, z, and β with different noise levels are shown in Table II.

As depicted in Table II, the amplitude of average normalized misfit values for gravity responses (5), depth (6), and β (7) remain minor and consistent, even after introducing noise into the test data. For instance, a marginal increase in misfit values occurs in response to an increase in noise intensity, thereby indicating the commendable stability and noise resistance of the well-trained deep neuron network. Moreover, the training

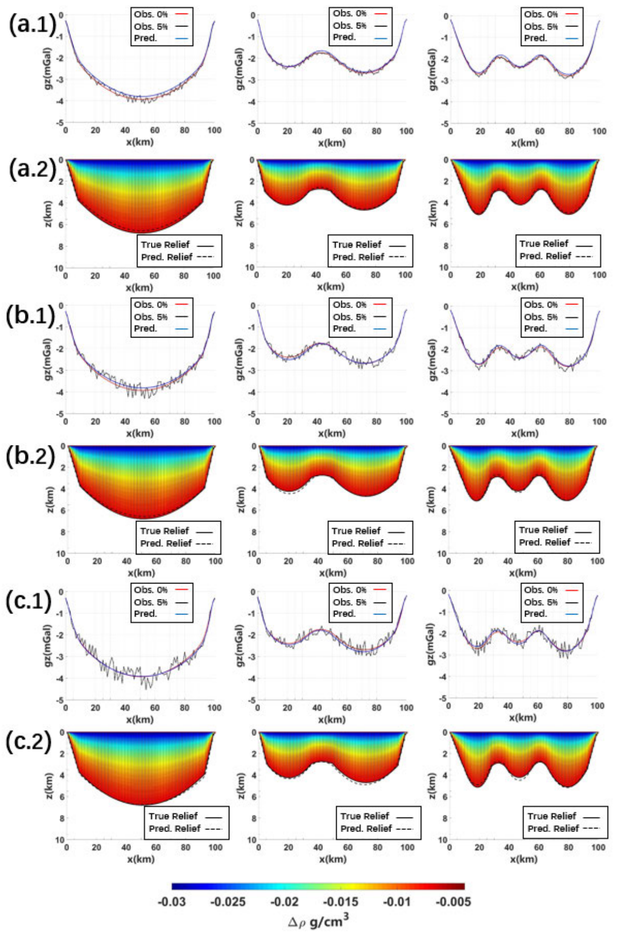

Fig. 7. Fitting behaviors and inversion results recovered by the proposed trained deep neuron network using three different noise levels for the three different graben-horned sedimentary basin models shown in Fig. 4. Comparison of: (a-1) observed and predicted gravity responses and (a-2) predicted reliefs and densities transferred by the recovered empirical parameters (β) against 5% Gaussian noise. Comparison of: (b-1) observed and predicted gravity responses and (b-2) predicted reliefs and density transferred by β against 10% Gaussian noise. Comparison of: (c-1) observed and predicted gravity responses and (c-2) predicted reliefs and density transferred by β against 15% Gaussian noise.

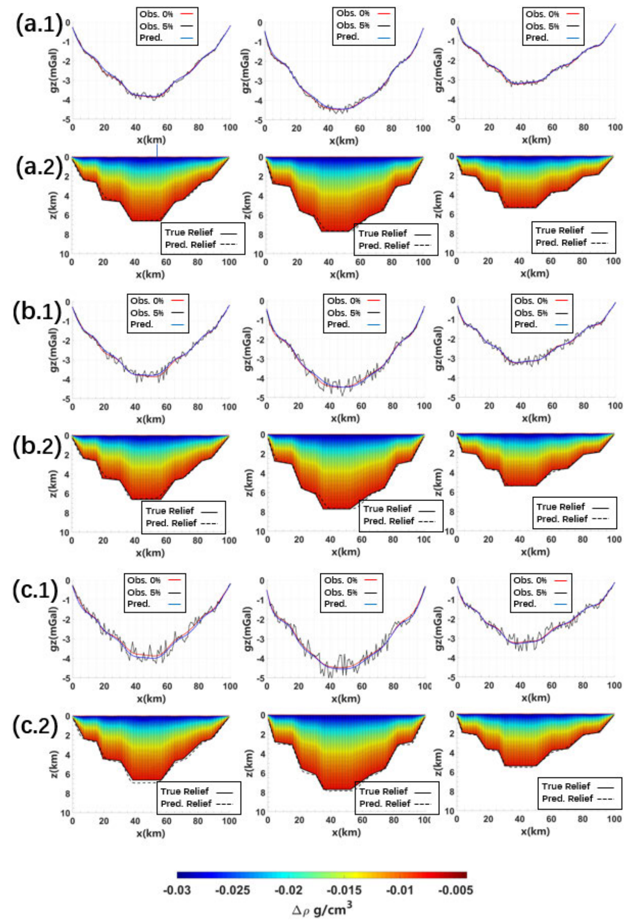

Fig. 8. Fitting behaviors and inversion results recovered by the proposed trained deep neuron network using three different noise levels for the three different rift sedimentary basin models shown in Fig. 5. Comparison of: (a-1) observed and predicted gravity responses and (a-2) predicted reliefs and density transferred by the recovered empirical parameters (β) against 5% Gaussian noise. Comparison of: (b-1) observed and predicted gravity responses and (b-2) predicted reliefs and density transferred by β against 10% Gaussian noise. Comparison of: (c-1) observed and predicted gravity responses and (c-2) predicted reliefs and density transferred by β against 15% Gaussian noise.

TABLE III
HYPERPARAMETERS SETTING OF DEEP LEARNING NETWORKS

Network Parameters	Settings	Method
Hidden Layers	4	Empirical Evaluation
Optimizer	Adam	Empirical Evaluation
Activation Function	Leaky ReLU	Empirical Evaluation
Learning Rate	0.001	Heuristics
Regularized Dropout	20%	Heuristics
Batch Size	256	Heuristics
Epoch	4,000	Early Stopping

computation times for the grab-horned sedimentary basin are recorded as 3.97, 3.88, and 3.64 min, respectively. In parallel, the training durations for the rift sedimentary basin amount to 3.37, 3.30, and 3.24 min, respectively. Interestingly, the data training duration decreases as the noise intensity escalates. The primary reason for this inverse relationship is that the widespread variation in the training data may expedite the convergence of the loss function (4), thereby negating the need for the network to update weighting and threshold parameters for further minimization of the loss function. The detailed hyperparameter settings are shown in Table III.

In contemplation of potential deviations between input data utilized in the training phase and actual case data, we generate an additional four models for each sedimentary type, presenting varied profile lengths (i.e., 40 and 80 km) along the x-axis. Given the fixed number of outputs, the width of the prisms in each model inevitably varies. The corresponding inversion outcomes are displayed in Fig. 9. These results indicate that the well-tuned DNN maintains commendable generality, effectively recovering both the interface and the density—as determined by the predicted empirical parameter β—even when faced with diverse prismatic sources.

IV. CASE STUDY

A. Geological Setting

The Poyang Basin, found in northern Jiangxi Province, China, in the vicinity of 115°30′–117°00′ E and 28°20′–29°30′ N (refer to the left panel in Fig. 10), is a fault-depression basin superimposed on Paleozoic strata,

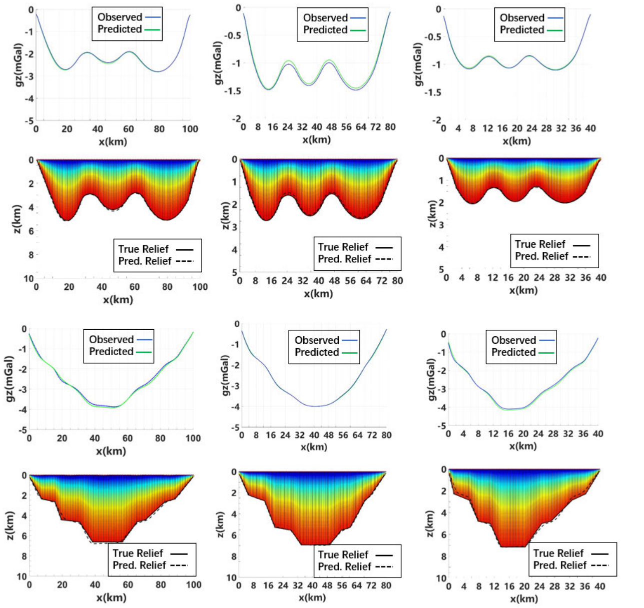

Fig. 9. (Top row) Comparison of predicted and observed vertical gravity g_z of three different graben-horned sedimentary basin models with total profile lengths as 100, 80, and 40 km. (Bottom row) Prediction and actual reliefs and density transferred by the recovered empirical parameters β for the three corresponding graben-horned sedimentary basin models.

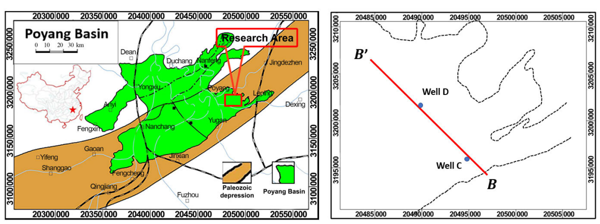

Fig. 10. (Left) Location of the case study is in the Poyang Basin. (Right) 2-D vertical gravity and seismic data acquired along red survey line B–B′ throughout two validation well-logging C and D.

thought to have taken shape during the Mesozoic and Cenozoic periods. Spanning an irregularly distributed area of approximately 11 230 km^2 in a northerly to east-northeasterly direction, the basin hosts five major river systems, culminating in the creation of Poyang Lake in the eastern portion of the basin, which covers a sizable area of 3050 km^2.

The structural configuration of the upper Paleozoic is largely determined by the NW-SE compression stress field from the Indosinian-Early Yanshanian era. Situated south of the Nanchang-Boyang line, the southern Poyang depression overlays the Pingxiang-Leping depression, a product of the upper Paleozoic–Triassic marine–terrestrial interactions and associated deposits. Prominent thrusts and folds are observable in the upper Paleozoic strata, while the rifts mainly manifest as NEE and NE reverse faults, complemented by NNE and NW left-lateral strike-slip faults. Key reverse faults that emerged in the early Mesozoic architecture, influenced by the late Yanshanian extension, were reversed into tensional normal faults and directed the deposition of Cretaceous sediments in the depression. Consequently, the Mesozoic structural scheme, to a degree, continues the early architectural framework, barring the rifts which predominantly appear as NEE and NE normal faults.

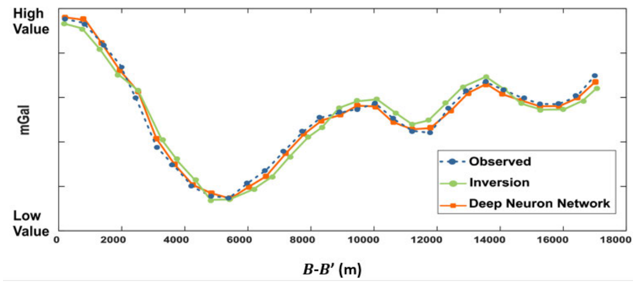

Fig. 11. Comparison of the observed and predicted vertical gravity responses from the traditional smooth inversion and deep neutron network.

The South Poyang depression comprises two main sectors: the western and eastern zones. Proceeding from NW to SE, the eastern zone consists of several minor structural entities, including the Nanjing depression, the Ruihong uplift, and the Erjiacun depression. The focus of this investigation is an NE-oriented, 1120-km^2 section of the Erjiacun depression, delineated by the boundary fault and the southern edge of the Ruihong metamorphic rock exposure, which is where the gravity data for this study was gathered. The predominant Mesozoic formations are the late Cretaceous Ganzhou Group and Guifeng Group. The depression encompasses three Mesozoic graben-style subsags, interspersed with uplifts. Presently, the main fault exerts a significant influence on the tectonic formation. This formation exhibits a thickness of approximately 1000 m, with the deep sags exceeding 3000 m at their maximum points. The middle–upper Paleozoic strata, with a residual thickness surpassing 1000 m, constitute a considerable fraction of this depression and represent the largest upper Paleozoic residual zone in the eastern segment of the South Poyang depression. During the Indosinian-Early Yanshan period, sections of the upper Paleozoic strata were folded and overturned, thereby persisting in an elevated position over an extended timeframe and undergoing sustained erosion. Seismic interpretation reveals substantial denudation of numerous upper Paleozoic locations. An examination of the geological outcrop characteristics in this area indicates that the upper Triassic and lower Jurassic are confined to a limited region within the remnant structural syncline.

B. Results and Interpretation

Employing vertical gravity field data distributed along an aggregate length of 17 km, with an approximate spacing of 0.5 km, we leverage the proposed DNN to reconstruct the basement relief. Our 2-D sedimentary model is partitioned into 100 discrete 2-D vertical rectangles, each with a width of 180 m. To illustrate the efficacy of the proposed methodology, a comparison is executed using traditional smooth inversion as a benchmark. The matching behaviors are exhibited in Fig. 11. The visualization clearly indicates that the predicted vertical gravity responses from both methods align favorably with the observed data.

Fig. 12 illustrates a comparative vertical cross section, juxtaposing the results derived from conventional inversion and the trained DNN. This comparison is superimposed onto the cross section of the seismic image drawn along line B–B′, passing through wells C and D, respectively. The interface

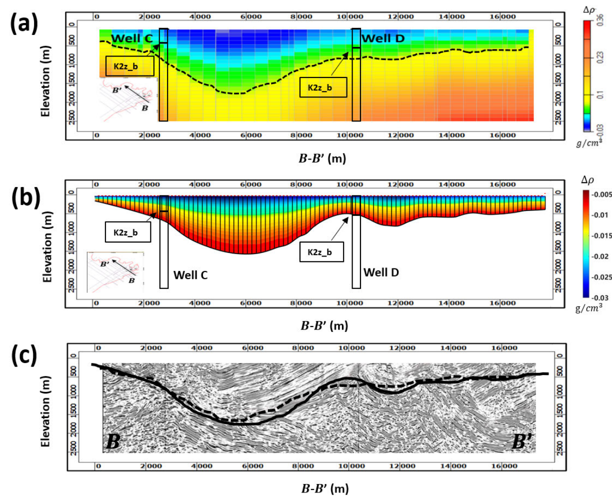

Fig. 12. Comparison of prediction relief by: (a) 2-D smooth inversion; (b) deep neutron network and actual results of rift sedimentary basin; and (c) seismic imaging section along the line B–B′, overlapping with the two curves of the recovered relief.

of the depression, as depicted on the left side of the seismic imaging [Fig. 12(c)], corresponds well with the smooth relief model reconstructed by the robustly trained DNN [Fig. 12(b)], as indicated by the black solid line. A similar, though less precise, correspondence is evident with the relief model recovered via the conventional inversion method [Fig. 12(a)], delineated by the black dashed line.

When evaluated in terms of density, a conspicuous peak in visual intensity manifests within the anomalous density recovered by conventional inversion, positioned between the green and yellow bands in the standard jet color bar, corresponding to a density contrast value of 0.075 g/cm^3. However, an examination of the maximum anomalous density recovered by the robustly trained DNN in the vicinity of the depression interface reveals a value of approximately -0.006 g/cm^3. This exhibits a noticeable deviation from the density derived through traditional inversion. The principal cause of this disparity in density can be traced to the divergent density recovery strategies employed by the two methods. Conventional inversion endeavors to recover the density across the entire space, whereas the robustly trained DNN focuses solely on recovering the density above the interface, operating under the assumption that the background density is 0 g/cm^3.

However, it appears that the traditional smooth inversion cannot detect the subsag on the right side, which is noteworthy given the outcomes the trained DNN has foreseen. To better validate the effectiveness of the algorithm, we overlap the wells C and D with the strata marker for K2z_b (interface of the Cretaceous basement) on the cross sections produced by the conventional and DNN, respectively [shown in Fig. 12(a) and (b)]. Upon contrasting the relief profile retrieved through conventional inversion methods with that predicted by the DNN, it emerges that the DNN prediction exhibits a more favorable correspondence with the strata marker at well D. The DNN's prediction for well C's alignment with the base interface, while not demonstrating the same degree of agreement as observed for well D, nonetheless surpasses the level of accuracy achieved by traditional inversion methods. We would like to underline that the seismic structure and well logging data are only used for validation after inversions and are not used as a priori knowledge to restrictions throughout the two inversion methods.

To summarize, the DNN approach substantiates its merit through a number of salient advantages in the real case. This encompasses a refined precision, courtesy of the method's unique focus on recovering density above the interface, offering an elevated granularity in pertinent regions. Its inherent resistance to Gaussian noise enhances the robustness, bolstering the reliability of results even in the presence of real-world noise contamination. A paramount strength of the DNN method lies in its capacity to anticipate nuanced geological features, as exemplified by the identification of the subsag in this study, highlighting its potential to discern details that traditional inversion methods may not capture. Its commendable alignment with the strata marker for the K2z b interface further endorses its proficiency in accurately delineating geological structures. Collectively, these distinguishing strengths elevate our DNN method as a potent instrument for intricate and precise geological analysis.

V. Conclusion

Exhibiting profound capabilities in implicitly learning intricate and nonlinear input–output model mappings, the DNN adjusts the thresholds and weights associated with adjoining layers through the gradient descent method. This is accomplished without the necessity of revealing the mathematical equations that physically articulate the relationship. The DNN proposed herein holds considerable potential for application in forecasting the bottom relief of sedimentary basement boundaries.

In the synthetic study, we enhance the assessment of the trained network's robustness by introducing zero-mean Gaussian noise of 5%, 10%, and 15%, respectively, to the synthetic input training datasets. It becomes apparent that the normalized misfit labels of the DNN remain consistent, irrespective of the imposed noise levels. The derived empirical parameters β can be nearly entirely reconstructed and subsequently translated into density. On a separate note, the discrepancies between the predicted and actual reliefs in the simulation datasets maintain a scale within the order of tens of meters. This discrepancy is virtually negligible when compared to the depth of a sedimentary basin, which spans several thousands of meters.

In the context of practical field application, the suggested DNN demonstrates robust efficiency in the prediction of both density and reliefs of the primary depression and subsag within the Poyang basin. This is particularly significant where traditional inversion falls short in capturing the intricacies of relief undulation, notably for the subsag. It bears highlighting that the inversion result from the DNN is further validated by the finite well-based stratigraphic information and corresponding seismic structure, exhibiting a notable fit.

Through a process markedly divergent from conventional inversion methods, which lean heavily on explicit a priori knowledge or assumptions, the DNN has the capacity to amplify the precision of geophysical imaging by deciphering inherent patterns and complexities ingrained within the dataset. Crucially, despite the foundational role of prior knowledge in forming the training data, it is essential to recognize that the operational functioning of the DNN is not dictated or restrained by explicit assumptions or models. Rather, the DNN acquires the capacity to generate predictions based on patterns discerned within the training data, thereby potentially uncovering intricate features or associations unaddressed by traditional inversion methodologies. Furthermore, the caliber and heterogeneity of the input training data can substantially impact the precision of the resultant output. Hence, notwithstanding the significant advantages offered by the DNN approach, it concurrently presents unique complexities and considerations.

Appendix

According to the forward propagation, as the input of the ith neuron in layer l, $\mathrm{net}_i^{(l)}$ can be expressed as

$$\mathrm{net}_i^{(l)}(\psi) = \sum_{j=1}^{sl-1} W_{ji}^{(l)} h_j^{(l-1)} + b_i^{(l)} \tag{A-1}$$

where $W_{ji}^{(l)}$ is the weight connecting the jth neuron in the layer $l-1$ and the ith neuron in layer l, where $b_i^{(l)}$ is defined as the bias; and $h_j^{(l-1right)}$ is the output of the jth neuron in layer $l-1$ as

$$h_j^{(l-1)} = f\left(\mathrm{net}_j^{(l-1)}(\psi)\right) \tag{A-2}$$

where $f(\cdots)$ is defined as activation function. Referring with (A-1), $\mathrm{net}_i^{(l-1)}(\psi)$ is the input of the jth neuron in the layer $l-1$.

The partial derivative of the weights $W_{ji}^{(L)}$ linking the jth neuron in the layer $L-1$ and the ith neuron in the last output layer L is expressed as

$$\begin{aligned}\frac{\partial E(\psi)}{\partial W_{ji}^{(L)}} &= \frac{\partial E(\psi)}{\partial O_k(\psi)} \frac{\partial O_k(\psi)}{\partial \mathrm{net}_i^{(L)}(\psi)} \frac{\partial \mathrm{net}_i^{(L)}(\psi)}{\partial W_{ji}^{(L)}} \\ &= -(T_k(\psi) - O_k(\psi)) \frac{\partial z_k(\psi)}{\partial \mathrm{net}_i^{(L)}(\psi)} h_j^{(L-1)}.\end{aligned} \tag{A-3}$$

It is worth noting that the output of the L layer (e.g., $h_j^{(L)}$) is the predicted value of depth information defined as $O_k(\psi)$ as

$$O_k(\psi) = h_j^{(L)} = f\left(\mathrm{net}_j^{(L)}(\psi)\right). \tag{A-4}$$

Hence, (A-3) can be rewritten as follows:

$$\begin{aligned}\frac{\partial E(\psi)}{\partial W_{ji}^{(L)}} &= \frac{\partial E(\psi)}{\partial z_k(\psi)} \frac{\partial O_k(\psi)}{\partial \mathrm{net}_i^{(L)}(\psi)} \frac{\partial \mathrm{net}_i^{(L)}(\psi)}{\partial W_{ji}^{(L)}} \\ &= -(T_k(\psi) - O_k(\psi)) f'\left(\mathrm{net}_j^{(L)}(\psi)\right) h_j^{(L-1)}\end{aligned} \tag{A-5}$$

set

$$\begin{aligned}\eta_k^{(L)} &= \frac{\partial E(\psi)}{\partial O_k(\psi)} \frac{\partial O_k(\psi)}{\partial \mathrm{net}_i^{(L)}(\psi)} \\ &= -(T_k(\psi) - O_k(\psi)) f'\left(\mathrm{net}_j^{(L)}(\psi)\right).\end{aligned} \tag{A-6}$$

Hence, the partial derivative of the weights $W_{ji}^{(L)}$ with respect to the cost function $E(\psi)$ can be rewritten as

$$\frac{\partial E(\psi)}{\partial W_{ji}^{(L)}} = \eta_k^{(L)} h_j^{(L-1)}. \tag{A-7}$$

Similarity, the gradient of the bias can be expressed as

$$\frac{\partial E(\psi)}{\partial b_i^{(L)}} = \frac{\partial E(\psi)}{O_k(\psi)} \frac{O_k(\psi)}{\partial \mathrm{net}_i^{(L)}(\psi)} \frac{\partial net_i^{(L)}(\psi)}{\partial b_i^{(L)}} = \eta_k^{(L)}. \tag{A-8}$$

According to the chain derivative method, for hidden layer $L-1$ layer

$$\begin{aligned}\frac{\partial E(\alpha)}{\partial W_{ji}^{(L-1)}} &= \frac{\partial E(\psi)}{O_k(\psi)} \frac{O_k(\psi)}{\partial \mathrm{net}_i^{(L)}(\psi)} \frac{\partial \mathrm{net}_i^{(L)}(\psi)}{\partial W_{ji}^{(L-1)}} \\ &= \eta_k^{(L)} W_{ji}^{(L)} \frac{\partial h_j^{(L-1)}(\psi)}{\partial W_{ji}^{(L-1)}}\end{aligned} \tag{A-9}$$

$$\begin{aligned}\frac{\partial h_j^{(L-1)}(\psi)}{\partial W_{ji}^{(L-1)}} &= \frac{\partial h_j^{(L-1)}(\psi)}{\partial \mathrm{net}_i^{(L-1)}(\psi)} \frac{\partial \mathrm{net}_i^{(L-1)}(\psi)}{\partial W_{ji}^{(L-1)}} \\ &= f'\left(\mathrm{net}_i^{(L-1)}(\psi)\right) h_j^{(L-2)}\end{aligned} \tag{A-10}$$

$$\frac{\partial E(\psi)}{\partial W_{ji}^{(L-1)}} = \eta_k^{(L)} W_{ji}^{(L)} f'(\mathrm{net}_i^{(L-1)}(\psi)) h_j^{(L-2)}. \tag{A-11}$$

Similarity, the gradient of the bias can be expressed as

$$\begin{aligned}\frac{\partial E(\psi)}{\partial b_i^{(L-1)}} &= \frac{\partial E(\psi)}{O(\psi)} \frac{O_k(\psi)}{\partial \mathrm{net}_i^{(L)}(\psi)} \frac{\partial \mathrm{net}_i^{(L)}(\psi)}{\partial b_i^{(L-1)}} \\ &= \eta_k^{(L)} W_{ji}^{(L)} \frac{\partial h_j^{(L-1)}(\psi)}{\partial b_i^{(L-1)}}\end{aligned} \tag{A-12}$$

$$\begin{aligned}\frac{\partial h_j^{(L-1)}(\psi)}{\partial b_i^{(L-1)}} &= \frac{\partial h_j^{(L-1)}(\psi)}{\partial \mathrm{net}_i^{(L-1)}(\psi)} \frac{\partial \mathrm{net}_i^{(L-1)}(\psi)}{\partial b_i^{(L-1)}} \\ &= f'\left(\mathrm{net}_i^{(L-1)}(\psi)\right)\end{aligned} \tag{A-13}$$

$$\frac{\partial E(\psi)}{\partial b_i^{(L-1)}} = \eta_k^{(L)} W_{ji}^{(L)} f'(\mathrm{net}_i^{(L-1)}(\psi)). \tag{A-14}$$

Acknowledgment

The authors thank the Changchun University of Science and Technology, Changchun, China, and the Chengdu University of Technology, Chengdu, China. They acknowledge the Engineering Geology Brigade of Jiangxi Bureau of Geology, Nanchang, China, and the Jiangxi Institute of Shale Gas Investigation and Development Research, Nanchang, for providing the gravity and related data.

References

[1] T. P. Yegorova, R. A. Stephenson, V. G. Kozlenko, V. I. Starostenko, and O. V. Legostaeva, "3-D gravity analysis of the Dniepr–Donets basin and donbas foldbelt, Ukraine," *Tectonophysics*, vol. 313, nos. 1–2, pp. 41–58, Nov.10, 1999.

[2] L. Nielsen and B. H. Jacobsen, "Integrated gravity and wide-angle seismic inversion fortwo-dimensional crustal modelling," *Geophys. J. Int.*, vol. 140, no. 1, pp. 222–232, Jan. 2000.

[3] G. Y. Yang, J. H. Wang, and H. Z. Yan, "Application of modeling inversion of Bouguer gravity anomalies to oil and gas exploration in the Erlian basin," *Chin. J. Geophys.-Chin. Ed.*, vol. 62, no. 1, pp. 316–330, Jan. 2019.

[4] L. Uieda and V. C. F. Barbosa, "Fast nonlinear gravity inversion in spherical coordinates with application to the south American moho," *Geophys. J. Int.*, vol. 208, no. 1, pp. 162–176, Jan. 2017.

[5] J. B. C. Silva, D. F. Santos, and K. P. Gomes, "Fast gravity inversion of basement relief," *Geophysics*, vol. 79, no. 5, pp. G79–G91, Sep./Oct. 2014.

[6] X. Feng, W. Wang, and B. Yuan, "3D gravity inversion of basement relief for a rift basin based on combined multinorm and normalized vertical derivative of the total horizontal derivative techniques," *Geophysics*, vol. 83, no. 5, pp. G107–G118, Sep./Oct. 2018.

[7] M. S. Chauhan, M. Fedi, and M. K. Sen, "Gravity inversion by the multi-homogeneity depth estimation method for investigating salt domes and complex sources," *Geophys. Prospecting*, vol. 66, no. S1, pp. 175–191, Mar. 2018.

[8] M. An and M. Assumpção, "Crustal and upper mantle structure in the intracratonic Paraná Basin, SE Brazil, from surface wave dispersion using genetic algorithms," *J. South Amer. Earth Sci.*, vol. 21, no. 3, pp. 173–184, Jul. 2006.

[9] J. L. G. Pallero, J. L. Fernández-Martínez, S. Bonvalot, and O. Fudym, "Gravity inversion and uncertainty assessment of basement relief via particle swarm optimization," *J. Appl. Geophys.*, vol. 116, pp. 180–191, May 2015.

[10] Y. L. Ekinci, Ç. Balkaya, G. Göktürkler, and Ş. Özyalın, "Gravity data inversion for the basement relief delineation through global optimization: A case study from the Aegean graben system, western anatolia, Turkey," *Geophys. J. Int.*, vol. 224, no. 2, pp. 923–944, Nov. 2020.

[11] L. I. Rudin, S. Osher, and E. Fatemi, "Nonlinear total variation based noise removal algorithms," *Phys. D: Nonlinear Phenomena*, vol. 60, nos. 1–4, pp. 259–268, Nov. 1992.

[12] D. F. Santos, J. B. C. Silva, C. M. Martins, R. D. C. S. dos Santos, L. C. Ramos, and A. C. M. de Araújo, "Efficient gravity inversion of discontinuous basement relief," *Geophysics*, vol. 80, no. 4, pp. G95–G106, Jul./Aug. 2015.

[13] J. Liu, and J. Zhang, "Structure-guided gravity inversion for layered density modeling with an application in the Chezhen Depression, Bohai Bay Basin," *Geophysics*, vol. 87, no. 1, pp. 1–54, 2021.

[14] M. S. Zhdanov and W. Lin, "Adaptive multinary inversion of gravity and gravity gradiometry data," *Geophysics*, vol. 82, no. 6, pp. Q101–Q114, Nov./Dec. 2017.

[15] K. Gessner, L. A. Gallardo, F. Wedin, and K. Sener, "Crustal structure of the northern menderes massif, western turkey, imaged by joint gravity and magnetic inversion," *Int. J. Earth Sci.*, vol. 105, no. 7, pp. 2133–2148, Oct. 2016.

[16] M. Jorgensen, and M. Zhdanov, "Application of Gramian and focusing structural constraints to joint inversion of gravity and magnetic data," in *Proc. 3rd Conf. Geophys. Mineral Explor. Mining*, 2020, pp. 1–4.

[17] Z. Xu, R. Wang, W. Xiong, J. Wang, and D. Wang, "3-D hybrid imaging based on gravity migration and regularized focusing inversion to predict the Poyang basin interface," *Geophysics*, vol. 86, no. 4, pp. 1–46, 2021.

[18] A. Jamasb, S.-H. Motavalli-Anbaran, and K. Ghasemi, "A novel hybrid algorithm of particle swarm optimization and evolution strategies for geophysical non-linear inverse problems," *Pure Appl. Geophysics*, vol. 176, no. 4, pp. 1601–1613, Apr. 2019.

[19] C. Braitenberg, M. Zadro, J. Fang, Y. Wang, and H. T. Hsu, "The gravity and isostatic moho undulations in Qinghai–Tibet plateau," *J. Geodynamics*, vol. 30, no. 5, pp. 489–505, Dec. 2000.

[20] M. S. Zhdanov, *Integral Transforms in Geophysics*. Berlin, Germany: Springer, 2012.

[21] T. A. Elkins, "The second derivative method of gravity interpretation," *Geophysics*, vol. 16, no. 1, pp. 29–50, 1951.

[22] L. J. Peters, "The direct approach to magnetic interpretation and its practical application," *Geophysics*, vol. 14, no. 3, pp. 290–320, 1949.

[23] M. H. P. Bott, "The use of rapid digital computing methods for direct gravity interpretation of sedimentary basins," *Geophys. J. Int.*, vol. 3, no. 1, pp. 63–67, Mar. 1960.

[24] D. W. Oldenburg, "The inversion and interpretation of gravity anomalies," *Geophysics*, vol. 39, no. 4, pp. 526–536, 1974.

[25] R. L. Parker and S. P. Huestis, "The inversion of magnetic anomalies in the presence of topography," *J. Geophys. Res.*, vol. 79, no. 11, pp. 1587–1593, Apr. 1974.

[26] M. Fedi and A. Rapolla, "3-D inversion of gravity and magnetic data with depth resolution," *Geophysics*, vol. 64, no. 2, pp. 452–460, Mar./Apr. 1999.

[27] G. Florio, "Mapping the depth to basement by iterative rescaling of gravity or magnetic data," *J. Geophys. Res., Solid Earth*, vol. 123, no. 10, pp. 9101–9120, Oct. 2018.

[28] G. E. Hinton and J. McClelland, "Learning representations by recirculation," in *Proc. Neural Inf. Process. Syst.*, 1987.

[29] J. Li, J.-H. Cheng, J.-Y. Shi, and F. Huang, "Brief introduction of back propagation (BP) neural network algorithm and its improvement," in *Advances in Computer Science and Information Engineering*. Berlin, Germany: Springer, 2012, pp. 553–558.

[30] Z. Dailei, H. Danian, and Z. Chong, "Application of BP neural network based on genetic algorithm in the inversion of density interface," *J. Jilin Univ., Earth Sci. Ed.*, vol. 47, no. 62, pp. 580–588, 2017.

[31] S. He, H. Cai, S. Liu, J. Xie, and X. Hu, "Recovering 3D basement relief using gravity data through convolutional neural networks," *J. Geophys. Res., Solid Earth*, vol. 126, no. 10, Oct. 2021, Art. no. e2021JB022611.

[32] X. Chen, Y. Du, Z. Liu, W. Zhao, and X. Chen, "Inversion of density interfaces using the pseudo-backpropagation neural network method," *Pure Appl. Geophys.*, vol. 175, no. 12, pp. 4427–4447, Dec. 2018.

[33] X. L. Feng, W. Y. Wang, F. Q. Liu, J.-G. Li, and B.-L. Lu, "2D gravity inversion of basement relief of rift basin based on a dual interface model," *Chin. J. Geophys.-Chin. Ed.*, vol. 57, no. 6, pp. 1934–1945, Jun. 2014.

[34] V. A. Litinsky, "Concept of effective density: Key to gravity depth determinations for sedimentary basins," *Geophysics*, vol. 54, no. 11, pp. 1474–1482, Nov. 1989.

[35] J. B. Silva, D. C. Costa, and V. C. Barbosa, "Gravity inversion of basement relief and estimation of density contrast variation with depth," *Geophysics*, vol. 71, no. 5, pp. J51–J58, Sep. 2006.

[36] A. Raiche, "A pattern recognition approach to geophysical inversion using neural nets," *Geophys. J. Int.*, vol. 105, no. 3, pp. 629–648, Jun. 1991.

[37] A. Arif, V. Sagayan, and M. N. Bin Karsiti, "Geophysical inversion using multilayer perceptron," in *Proc. IEEE Student Conf. Res. Develop. (SCOReD)*, Nov. 2009, pp. 93–96.

[38] D. Hall, "Classification of cued metalmapper data using data mining techniques," in *Proc. 27th Annu. Symp. Appl. Geophys. Eng. Environ. Problems (SAGEEP)*. European Association of Geoscientists & Engineers, Mar. 2014, p. cp-400.

[39] L. Y. Zhang and H. F. Liu, "The application of ABP method in high?Density resistivity method inversion," *Chin. J. Geophys.*, vol. 54, no. 1, pp. 64–71, 2011.

[40] C. Calderón-Macías, M. K. Sen, and P. L. Stoffa, "Artificial neural networks for parameter estimation in geophysics [link]," *Geophys. Prospecting*, vol. 48, no. 1, pp. 21–47, 2000.

[41] N. Srivastava, G. Hinton, A. Krizhevsky, I. Sutskever, and R. Salakhutdinov, "Dropout: A simple way to prevent neural networks from overfitting," *J. Mach. Learn. Res.*, vol. 15, pp. 1929–1958, Jun. 2014. [Online]. Available: http://jmlr.org/papers/v15/srivastava14a.html

Rui Wang received the Ph.D. degree in traffic and transportation engineering from Jilin University, Changchun, China, in 2014.

He is currently an Associate Professor and the Head of the Software Engineering Department, School of Computer Science and Technology, Changchun University of Science and Technology, Changchun. His main research interests include machine learning, computer vision, geophysics, and deep learning interpretation of continental dynamics.

Zhengwei Xu received the M.Sc. degree in geo-exploration science and information technology from Jilin University, Changchun, China, in 2008, and the Ph.D. degree in geophysics from The University of Utah, Salt Lake City, UT, USA, in 2013.

He is currently a Researcher with the College of Geophysics, Chengdu University of Technology, Chengdu, China. His research interests include gravity, magnetic, and electromagnetic forward modeling and inversion theory, as well as incorporation and joint inversion of multigeophysical data using artificial intelligence.

Changjie Lai received the B.S. degree in geophysics from Xi'an Shiyou University, Xi'an, China, in 2010, and the M.Sc. degree from the China University of Petroleum, Beijing, China, in 2013.

His research interests include basic geological survey and resource evaluation of unconventional oil and gas.

Xuben Wang received the Ph.D. degree in geophysics from the College of Geophysics, Chengdu University of Technology, Chengdu, China, in 2002.

He is currently a Senior Professor with the College of Geophysics and also the Director of the Key Laboratory of Earth Exploration and Information Technology, Ministry of Education, Chengdu University of Technology. His main research interests include magnetotellurics and airborne electromagnetic forward and inversion theory as well as the multiphysics interpretation of continental dynamics.

Dr. Wang is the Executive Director of Chinese Geophysical Society. He is also the Director of the Innovation Consortium for Geophysics and Continental Dynamics and a Senior Visiting Scholar of the Commonwealth Scientific and Industrial Research Organisation (CSIRO), Australia.

Michael S. Zhdanov (Member, IEEE) received the M.Sc. degree in geophysics from the Moscow Gubkin State University of Oil and Gas, Moscow, Russia, in 1968, and the Ph.D. degree in physics and mathematics from Moscow State University, Moscow, in 1970.

He was the Founding Director of the Geoelectromagnetic Research Institute, Russian Academy of Sciences, Moscow, and also the Deputy Director of the Institute of Terrestrial Magnetism, Ionosphere and Radio Wave Propagation. He is currently a Distinguished Professor with the Department of Geology and Geophysics, The University of Utah, Salt Lake City, UT, USA, the Director of the Consortium for Electromagnetic Modeling and Inversion (CEMI), and the CEO and the Chairperson of TechnoImaging, Salt Lake City. He is also an Honorary Gauss Professor with the Göttingen Academy of Sciences, Göttingen, Germany, and a Honorary Professor with the China National Centre for Geological Exploration Technology, Beijing, China. His research interests include fundamental and applied geophysics, inversion theory, electromagnetic theory and methods, as well as integration and joint inversion of multiphysics data.

Dr. Zhdanov is a fellow of the Russian Academy of Natural Sciences and the Electromagnetics Academy of USA, and a Honorary Member of the Society of Exploration Geophysicists.

Guowei Li, photograph and biography not available at the time of publication.

Zhiyao Cheng, photograph and biography not available at the time of publication.

Jun Li received the B.S., M.Sc., and Ph.D. degrees in geophysics from the Chengdu University of Technology, Changchun, China, in 2001, 2005, and 2010, respectively.

His research interests include fundamental and applied geophysics, inversion theory, gravity, and magnetic theory and methods.

Guangdong Zhao received the B.S. degree in prospecting technology and engineering from Chang'an University, Xi'an, China, in 2015, and the Ph.D. degree in geophysical prospecting and information technology from Central South University, Changsha, China, in 2021.

He is currently an Associate Researcher with the College of Geophysics, Chengdu University of Technology, Chengdu, China. His research interests include forward and inversion modeling methods of gravity and magnetic, with the application to lunar mascon basins and the Tibetan plateau.

Shengxian Liang received the B.S. degree in geophysics from the China University of Geosciences (Wuhan), Wuhan, China, in 2009. He is currently pursuing the Ph.D. degree with the Chengdu University of Technology, Chengdu, China.

His research interests include gravity and magnetic inversion imaging, geophysical exploration of solid minerals and oil and gas, and geodynamics.

Hua Li received the Ph.D. degree from the Changchun University of Science and Technology, Changchun, China, in 2017.

She is currently a Professor with the Changchun University of Science and Technology, where she is also the Director of the Department of Computer Science and Technology. She is mainly engaged in virtual reality, computer vision, and machine-learning-related research.

Yuxin Zhang received the Ph.D. degree from Hokkaido University, Sapporo, Japan, in 2012.

Since 2001, he has been with the Changchun University of Science and Technology, Changchun, China, where he is currently an Associate Professor with the Department of Computer Science and Technology. His research interests are in the areas of robust speech recognition in noisy environments.